OPEN ACCESS
IOP Publishing
Superconductor Science and Technology
Supercond. Sci. Technol. **36** (2023) 044004 (12pp)
https://doi.org/10.1088/1361-6668/acbeea

Thermal thin shell approximation towards finite element quench simulation

Erik Schnaubelt[1,2,*], **Mariusz Wozniak**[1] and **Sebastian Schöps**[2]

[1] CERN, Meyrin, Switzerland
[2] Technical University of Darmstadt, Darmstadt, Germany

E-mail: erik.schnaubelt@cern.ch

Received 30 September 2022, revised 13 February 2023
Accepted for publication 24 February 2023
Published 8 March 2023

Abstract

Superconducting electromagnets commonly exhibit thin layers with high aspect ratio such as insulation layers or turn-to-turn contacts. A finite element (FE) analysis of these devices can lead to unfavorable meshes in these thin layers, either because of a high number of degrees of freedom or mesh elements of poor quality which decrease the accuracy of the simulation results. To mitigate these issues when conducting a thermal FE analysis solving the heat equation, this work proposes to collapse thin volume layers into surfaces by using a thermal thin shell approximation (TSA). The proposed method uses one-dimensional Lagrange elements across the thickness of the thin layer and can handle a variety of interface conditions, multi-layered structures, heat sources, nonlinear material behavior or coupling to physics other than heat transfer. The efficiency of the proposed approximation is highlighted by comparison with a reference model with a conventionally meshed insulation for a model problem exhibiting a brick wall structure where a stationary heat equation is solved. The formulation is then verified against reference models with meshed insulation solving a transient heat equation for an insulated high-temperature superconductor pancake coil exhibiting a local defect which causes a thermal runaway. The benefit of using the model with the TSA is studied by analyzing pancake coils with different ratios of the insulation layer to the coated conductor thickness. It is shown that the smaller the ratio, the shorter the solution time and the lower the number of unknowns of the thin shell model when compared to the conventionally meshed insulation in order to reach the same numerical accuracy. The method is implemented in an open-source FE framework and a reference implementation for a simple model problem is shared alongside this paper.

Keywords: thermal thin shell approximation, thin layer, finite element method, quench simulation, open-source, electromagnet, high-temperature superconductor pancake coil

(Some figures may appear in colour only in the online journal)

* Author to whom any correspondence should be addressed.

1. Introduction

In order to aid the development and analysis of quench detection and protection methods for superconducting devices, appropriate numerical tools are needed (see, e.g. [1–3]). When using the finite element (FE) method, the small ratio of thickness of insulation or contact resistance layers to the thickness of the conductor can lead to numerical difficulties [4] since the accuracy of the method depends on the quality of the mesh [5, section 5.3]. As a consequence, manual effort needs to be spent in order to avoid the generation of mesh elements of poor quality, e.g. by using different element types in the thin layered regions. This commonly results in a high number of degrees of freedom (DoF) and requires additional time to suitably design and generate the mesh. Furthermore, these solutions depend on the considered geometry (see, e.g. [6] for canted cosine theta magnet geometries) and can only partially be used for solving other types of physics. As a consequence, in a typical simulation workflow, up to 75% of the overall required time is used for modeling geometry and its discretization [7].

Thus, it is desirable to find suitable methods to deal with thin layers. To this end, various so-called thin shell approximations (TSAs) have been proposed, e.g. for electromagnetic [8–12] and thermal [4, 13] problems. These methods collapse the volumetric thin layers into surfaces in the middle of the original layer, thus avoiding the need of a volumetric mesh representation. Appropriate conditions are enforced on the (two sides of the) surface in order to approximate the change of the fields across the thickness of the original layer.

In this paper, a general TSA to solve thermal problems related to quench phenomena in superconducting devices is proposed. Similar to [11] for the computation of eddy currents in thin superconducting sheets, one-dimensional (1D) Lagrange elements are used across the thickness of the thin shell. For temperature fields, this approach leads to a virtual discretization of the temperature inside the thin insulation layer using a three-dimensional (3D) tensor-product Lagrangian basis [14, section 1.2.4.] by multiplying two-dimensional (2D) Lagrange elements on the thin shell surface and 1D Lagrange elements across its thickness. This procedure requires no further approximations other than collapsing the volumetric insulation to a surface[3]. In particular, both the tangential heat flux, which is neglected by the so-called thermally-thick approximation (see, e.g. [16, section 2]), as well as the normal temperature gradient, which is first neglected in [13] and afterwards corrected for the specific case of yttrium barium copper oxide coated conductors (CC), can be represented in a straightforward manner. While COMSOL Multiphysics® [17] includes a proprietary mechanism to solve the problem, this paper proposes, to the best of our knowledge, the first general, open-source thermal TSA including a rigorous and detailed derivation. Furthermore, it is the first time that the proposed method is applied to models involving high-temperature superconductors (HTS).

The formulation for the model thermal problem, introduced in section 2, is derived and discussed in more detail in section 3. A reference, open-source implementation of the formulation is proposed in section 4 and can be found at [18]. Furthermore, in the same section, two model problems are solved which exhibit thin insulation layers which are discretized using the proposed TSA. First, a model consisting of four high thermally conducting bare parts connected with thin insulation highlights the decrease of the numerical accuracy with low mesh quality, even for seemingly simple geometries. It is shown that the proposed TSA is able to accurately solve the problem without additional effort for mesh creation or an elevated number of DoF.

Second, an insulated high-temperature superconducting pancake is considered which exhibits a local defect causing a thermal runaway. It is shown that the TSA correctly captures the evolution of the hot spot temperature over time, for different insulation thicknesses. Furthermore, the benefit of the proposed TSA in terms of reduced computational time and number of DoF as a function of the ratio of the insulation thickness to that of the bare conductor is discussed. It is shown that the smaller this ratio is, the more efficient the TSA is compared to conventionally meshed models if the same relative error in the maximum temperature is not to be exceeded. This is especially interesting for no-insulation (NI) HTS pancake coils where the latter ratio tends to vanish and a conventionally meshed insulation layer is not a practical alternative to a TSA.

Attention is paid to highlight the generality of the approach which is not only applicable to thin insulation layers in HTS applications, but also for other (potentially multi-layered) materials, different boundary conditions (BC) or heat sources in the thin layers, representing, e.g. quench heaters. The proposed approach is not restricted to insulated HTS magnets and can also be applied to other thermal problems (e.g. for electric machines). In particular, due to the close nature of the electromagnetic thin shell developed in [11] and the thermal thin shell presented in this work, a magneto-thermal coupled thin shell can be considered as well. The proposed TSA also enables the solution of problems where the thin layers cannot be practically resolved with a volumetric mesh, for example for the turn-to-turn thermal contact resistance of NI coils.

2. Problem definition: heat equation

As a simple 3D model problem to derive the proposed thermal thin shell formulation, a cuboidal domain consisting of a bare part Ω_b with thermal conductivity κ_b and an insulation layer Ω_i with thermal conductivity κ_i is considered. The geometry is shown in figure 1 and is referred to as model A1 (see table 1). The bare part is assumed to be a better thermal conductor than the insulation, i.e. $\kappa_\mathrm{b} \gg \kappa_\mathrm{i}$. The latter assumption is, however, not a limitation of the proposed method which can also handle tangential heat flux.

[3] This is due to the fact that the tensor-product Lagrangian basis spans suitable sub-spaces of the required gradient-conforming finite element spaces, see [14, section 1.2.4.] or [15, section 4.6.].

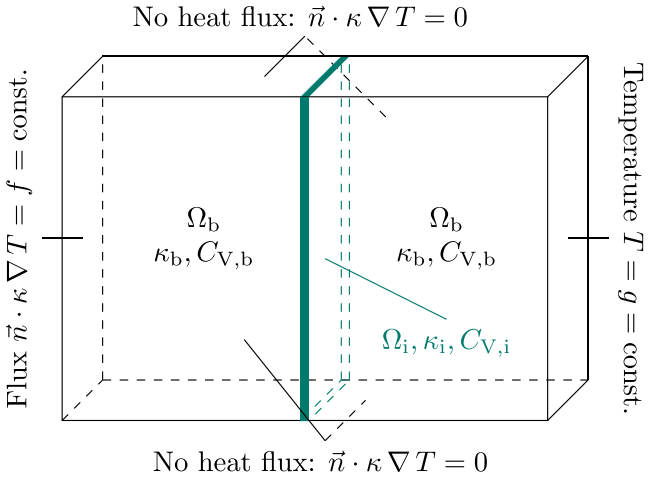

Figure 1. Model A1; non-homogeneous boundary conditions are applied on the left and right bounding surfaces while homogeneous Neumann conditions impose zero heat flux on all other bounding surfaces.

2.1. Strong formulation

In order to analyze the thermal behavior of the model problem, the heat balance equation is solved in the computational domain $\Omega = \Omega_\mathrm{i} \cup \Omega_\mathrm{b}$ with boundary $\partial\Omega$. It reads: find the temperature T such that:

$$-\nabla\cdot(\kappa\nabla T) + C_\mathrm{V}\,\partial_t T = Q \quad \text{in } \Omega, \tag{1}$$

$$\vec{n}_\Omega\cdot(\kappa\nabla T) = f \quad \text{on } \Gamma_\mathrm{neu}\subset\partial\Omega, \tag{2}$$

$$T = g \quad \text{on } \Gamma_\mathrm{dir}\subset\partial\Omega. \tag{3}$$

Herein, κ denotes the thermal conductivity, C_V the volumetric heat capacity, Q a heat source power density (e.g. Joule loss density), t the time, g an imposed boundary temperature, f an imposed boundary heat flux, $\vec{n}_\Omega$ the unit vector normal to $\partial\Omega$ and Γ denotes a surface.

2.2. Weak formulation

By multiplying the strong form (1) with a test function T', integration over the computational domain and partial integration, the weak problem is found after inserting the BC (2) and (3). It reads, find $T\in H^1_g(\Omega)$ such that [14, section 6.1.3.]:

$$\begin{aligned}(\kappa\nabla T,\nabla T')_\Omega + (C_\mathrm{V}\,\partial_t T, T')_\Omega - \langle f, T'\rangle_{\Gamma_\mathrm{neu}} \\ = (Q,T')_\Omega \;\forall T'\in H^1_0(\Omega)\,,\end{aligned} \tag{4}$$

where $H^1_g(\Omega)$ is the space of square integrable functions with square integrable weak gradient in Ω which fulfill the Dirichlet boundary condition (3). Furthermore, $(\cdot,\cdot)_\Omega$ denotes the volume integral in Ω of the scalar product of the two arguments while $\langle\cdot,\cdot'\rangle_{\Gamma_\mathrm{neu}}$ denotes the surface integral on Γ_neu of the two arguments.

3. Thin shell formulation

In this section, the formulation of the proposed TSA is introduced starting from the weak formulation (4).

3.1. Introduction of the internal problem

The insulation layer volume Ω_i is collapsed into a surface Γ_i in the middle of the original layer (see figure 2). This procedure removes the need for a volumetric mesh representation of Ω_i. Since T is not constant inside Ω_i, there is a temperature jump across the insulation and the thin shell method must also reproduce this temperature difference across Γ_i. To this end, two different temperatures T^- and T^+ (as well as test functions $T^{+\prime}$ and $T^{-\prime}$) with support restricted to $\Omega^-_{\mathrm{b,i}}$ and $\Omega^+_{\mathrm{b,i}}$ as shown in figure 2 are introduced, which represent the temperature on both sides of the shell surface.

The discontinuity of the temperature field can be introduced by either (i) using a duplication of mesh DoF to construct Γ^+_i and Γ^-_i as two sides of Γ_i allowing independent DoF for T^+ and T^- [11] or (ii) using dedicated FE basis functions with support restricted to one side of the shell surface [19]. While all models are implemented and reference implementations are provided for both approaches, only the second one is discussed in the remainder of the paper.

An interface condition on Γ_i is enforced by considering an additional surface contribution in the weak formulation (4), i.e.

$$\begin{aligned}(\kappa\nabla T,\nabla T')_{\Omega_{\mathrm{b,i}}} + (C_\mathrm{V}\,\partial_t T, T')_{\Omega_{\mathrm{b,i}}} - \langle f, T'\rangle_{\Gamma_\mathrm{neu}} \\ + \langle\vec{n}\cdot\kappa\nabla T, [T']\rangle_{\Gamma_\mathrm{i}} = (Q,T')_{\Omega_{\mathrm{b,i}}} \quad \forall T'\in H^1_0(\Omega)\,.\end{aligned} \tag{5}$$

Herein, $[T'] := T^{+\prime}|_{\Gamma_\mathrm{i}} - T^{-\prime}|_{\Gamma_\mathrm{i}}$ denotes the jump of T' across Γ_i and $\vec{n} = -\vec{n}^+ = \vec{n}^-$ is the unit vector normal to the thin shell (as illustrated in the right hand side of figure 2). The surface terms are now used for an internal discretization of the heat equation in $\hat{\Omega}_\mathrm{i}$. The latter is the internal domain representing the original insulation layer Ω_i as shown in figure 3.

Inside the virtual domain $\hat{\Omega}_\mathrm{i}$, the heat equation is solved to find $\hat{T}$ which approximates the temperature profile inside the insulation volume layer Ω_i. The internal problem in $\hat{\Omega}_\mathrm{i}$ and the external problem in $\Omega_{\mathrm{b,i}}$ are linked by enforcing that the temperatures $\hat{T}$ and T on Γ^+_i and Γ^-_i are identical for both problems, i.e. $\hat{T}|_{\Gamma^-_\mathrm{i}} = T|_{\Gamma^-_\mathrm{i}} = T^-$ and $\hat{T}|_{\Gamma^+_\mathrm{i}} = T|_{\Gamma^+_\mathrm{i}} = T^+$. Hence, for the sake of a concise notation, the symbol T is used as the unknown of both problems.

In summary, the internal weak problem in $\hat{\Omega}_\mathrm{i}$ reads:

$$\begin{aligned}\langle\vec{n}\cdot\kappa\nabla T, [T']\rangle_{\Gamma_\mathrm{i}} = -(Q,T')_{\hat{\Omega}_\mathrm{i}} + (\kappa\nabla T,\nabla T')_{\hat{\Omega}_\mathrm{i}} \\ + (C_\mathrm{V}\,\partial_t T, T')_{\hat{\Omega}_\mathrm{i}}\,.\end{aligned} \tag{6}$$

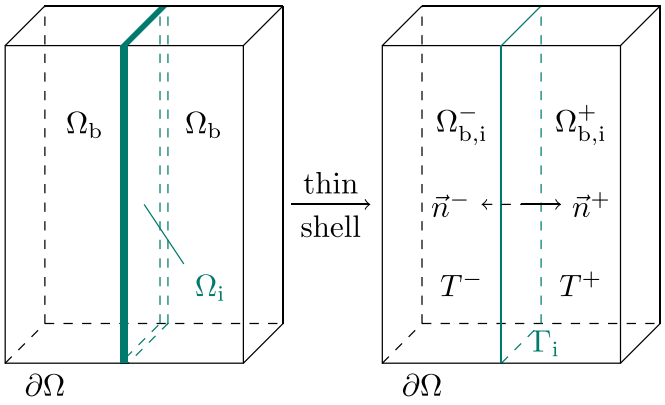

Figure 2. Model A1; in which, following the proposed approach, the thin insulation layer marked in green (left) is collapsed into a surface (right). This increases the volume of the bare part Ω_b by the volume of Ω_i creating $\Omega_{\mathrm{b,i}}$.

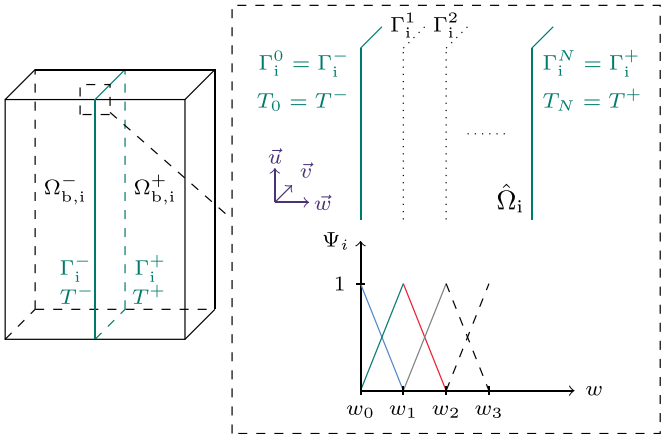

Figure 3. Model A1; in the proposed approach, the thin insulation layer is represented by a virtual domain $\hat{\Omega}_\mathrm{i}$ in which the heat equation is solved using 1D Lagrange elements along the thickness.

The first term is exactly the boundary term of the original weak formulation (5) which will later be used to insert the internal formulation into the external one.

3.2. FE discretization of the internal problem

The right hand side of the internal problem (6) is approximated by using a tensor-product based FE method. To this end, a local coordinate system $(\vec{u},\vec{v},\vec{w})$ is used in the following with $(\vec{u},\vec{v})$ oriented along the tangential and $\vec{w}$ oriented along the normal direction of Γ_i as shown in figure 3. As a first step, to build the mesh for the internal FE discretization, $\hat{\Omega}_\mathrm{i}$ is split into N auxiliary layers $\hat{\Omega}_\mathrm{i}^{(k)}$ with $\hat{\Omega}_\mathrm{i} = \bigcup_{k=1}^{N} \hat{\Omega}_\mathrm{i}^{(k)}$. We have $\hat{\Omega}_\mathrm{i}^{(k)} := \Gamma_\mathrm{i}^{(k)} \times [w_{k-1}, w_k]$ for $k = 1,\dots,N$ and $\hat{\Omega}_\mathrm{i} = \Gamma_\mathrm{i} \times [w_0, w_N]$. Hence, the 3D domain $\hat{\Omega}_\mathrm{i}$ is constructed as the Cartesian product of the 2D domain Γ_i and the 1D domain $[w_0, w_N]$. This enables us to approximate the temperature using a tensor-product polynomial basis [14, section 1.2.4.] in the following. Inserting all previous definitions in (6), we find:

$$\begin{aligned} &-(Q,T')_{\hat{\Omega}_\mathrm{i}} + (\kappa\nabla T, \nabla T')_{\hat{\Omega}_\mathrm{i}} + (C_\mathrm{V}\,\partial_t T, T')_{\hat{\Omega}_\mathrm{i}} \\ &\quad = \sum_{k=1}^{N} \Big\{ -(Q,T')_{\hat{\Omega}_\mathrm{i}^{(k)}} + (\kappa\nabla T, \nabla T')_{\hat{\Omega}_\mathrm{i}^{(k)}} \\ &\qquad + (C_\mathrm{V}\,\partial_t T, T')_{\hat{\Omega}_\mathrm{i}^{(k)}} \Big\}. \end{aligned} \tag{7}$$

The latter formulation is still comprised of volume integrals in $\hat{\Omega}_\mathrm{i}^{(k)}$. In order to decompose them into integrals over $\Gamma_\mathrm{i}^{(k)}$ and $[w_{k-1}, w_k]$, a product discretization of T inside $\hat{\Omega}_\mathrm{i}^{(k)}$ is assumed as:

$$T|_{\hat{\Omega}_\mathrm{i}^{(k)}}(u,v,w,t) = \sum_{j=k-1}^{k} T_j(u,v,t)\Psi_j(w). \tag{8}$$

Herein, $T_j := T|_{\Gamma_\mathrm{i}^{(j)}}$ denotes the temperature on $\Gamma_\mathrm{i}^{(j)}$ and enforcing $T_0 = T^-$ and $T_N = T^+$ links the internal and external problem (see also figure 3). Furthermore, $\Psi_j(w)$ denotes the basis functions along $\vec{w}$ which can be chosen according to the simulation needs. In this work, first-order Lagrange basis functions:

$$\Psi_{k-1}(w) = \frac{w_k - w}{w_k - w_{k-1}} \quad \text{and} \quad \Psi_k(w) = \frac{w - w_{k-1}}{w_k - w_{k-1}},$$

are used due to their generality and simplicity. This leads to a tensor-product Lagrangian discretization of the internal problem.

Using the same ansatz for the test function T' (Galerkin scheme) subsequently leads to a decomposition of the right hand side of the internal problem (7) into surface integrals over $\Gamma_\mathrm{i}^{(k)}$ and 1D FE matrices in $[w_{k-1}, w_k]$. The detailed derivation can be found in appendix A while only the final result is presented here. In summary, for $l = k-1, k$, the internal problem reads:

$$\begin{aligned} \langle \vec{n}\cdot\kappa\nabla T, [T']\rangle_{\Gamma_\mathrm{i}} = \sum_{k=1}^{N}\sum_{j=k-1}^{k} \Big\{ &\Big\langle S^{(k)}_{lj,\kappa}\, T_j, T'_l \Big\rangle_{\Gamma_\mathrm{i}^{(k)}} \\ &+ \Big\langle M^{(k)}_{lj,\kappa}\, \nabla T_j, \nabla T'_l \Big\rangle_{\Gamma_\mathrm{i}^{(k)}} \\ &+ \Big\langle M^{(k)}_{lj,C_\mathrm{V}}\, \partial_t T_j, T'_l \Big\rangle_{\Gamma_\mathrm{i}^{(k)}} \\ &- \Big\langle f^{(k)}_{l,Q}, T'_l \Big\rangle_{\Gamma_\mathrm{i}^{(k)}} \Big\}, \end{aligned} \tag{9}$$

where the 1D FE matrices:

$$\begin{aligned} S^{(k)}_{lj,\kappa} &:= \int_{w_{k-1}}^{w_k} \kappa\,\partial_w N_l\,\partial_w N_j\,\mathrm{d}w, \\ M^{(k)}_{lj,\kappa} &:= \int_{w_{k-1}}^{w_k} \kappa\, N_l N_j\,\mathrm{d}w, \\ M^{(k)}_{lj,C_\mathrm{V}} &:= \int_{w_{k-1}}^{w_k} C_\mathrm{V}\, N_l N_j\,\mathrm{d}w, \\ f^{(k)}_{l,Q} &:= \int_{w_{k-1}}^{w_k} Q N_l\,\mathrm{d}w, \end{aligned} \tag{10}$$

have been used. These integrals are computed either using Gaussian quadrature or, if element-wise constant material parameters and heat sources are assumed, are pre-computed analogously to [20, section 2.8.1.]. In particular, they can be evaluated without the need for a volumetric mesh representation of Ω_i.

The internal problem (9) is then inserted into the external problem (5) to yield the final formulation.

3.3. Final remarks and discretization

Since a FE discretization of the internal problem is used, classical BC, i.e. Dirichlet, Neumann or Robin conditions, can be considered in a straightforward manner on Γ_i^+ or Γ_i^- as well as internal heat sources in the thin layers. Furthermore, multi-layered domains Ω_i can be considered by increasing the number of auxiliary layers N. Let us also note that the proposed formulation can be used analogously for 2D models assuming transversal or axisymmetric symmetry.

Lowest-order Lagrange basis functions are used to discretize T as well as T_j and the corresponding test functions. In order to integrate the problem in time, fixed time-step, implicit Euler schemes or adaptive time-stepping using a second-order backward differentiation formula [21] are used.

4. Numerical examples

In this section, three numerical model problems will be discussed, see table 1 for a comprehensive overview. The proposed TSA is implemented in the open-source FE framework GetDP 3.4 [22] relying on the open-source software Gmsh 4.10.5 [23] for mesh creation. In particular, the Python application programming interface of Gmsh [24] is used to create the pancake coil geometry which is discussed in section 4.3. When the mesh DoF of Γ_i are duplicated rather than using one-sided supported basis functions, the duplication is done using the 'Crack' plugin [25], available in Gmsh.

4.1. Reference implementation

Model A1 is used to derive the proposed TSA in section 3. In addition, three slightly adapted cases A2, A3 and A4 are presented, each highlighting different features of the proposed TSA (compare table 1 and [18]). An open-source reference implementation of these four models is available at [18]. For all cases, both thin shell and volumetrically meshed insulation models are available, as well as an implementation using the one-sided supported basis functions or duplicated mesh surfaces.

Particular attention is paid to show the implementation of heat sources in the internal problem which can be used to model, e.g. quench protection heaters. Furthermore, it is shown how to impose BC on a thin shell touching the external model boundary. The documentation and code comments in the repository [18] contain more details and instructions on how to setup and solve the model problems. For all four models, the TSA and volumetrically meshed insulation reference models show excellent agreement with the relative error of the maximum temperature below 0.004% for all time steps. Due to the simplicity of the models, the same number of DoF can be used for both models to achieve accurate results. For conciseness, the results are not discussed further in this paper.

4.2. Brick wall model problem

As stated before, the quality of the FE mesh directly influences the accuracy of the FE approximation [5, section 5.3]. In this subsection, we will show the implications of poor mesh quality in thin volumetric layers for the accuracy of thermal solutions by investigating simple model problem B. It features four conductors arranged in a brick wall geometry as shown in figure 4. In order to highlight that inaccurate solutions are already obtained in these simple settings, transient effects will be neglected and linear material properties are assumed (table 2). To this end, pre-computed 1D matrices are used as detailed in [20, section 2.8.1.]. Since a single-material insulation layer is considered, the number of layers $N = 1$ is used.

The stationary heat equation problem is solved using five different meshes (compare figure 5); the first four with volumetric insulation layer. We consider (a) a very fine, structured mesh used as a reference solution, (b) a coarse, structured mesh, (c) a fine, unstructured mesh, (d) a coarse, unstructured mesh and (e) a mesh with the TSA. The shown meshes are extruded along the third dimension with low aspect ratio elements.

In order to create the structured meshes (a) and (b), the meshing software Gmsh uses user-defined constraints. From figure 5(d), it is apparent that the coarse unstructured mesh (d) results in elements of poor quality, characteristic for the high aspect ratio of the elements. The quality of the unstructured mesh can be increased by refining the mesh inside Ω_i as shown with mesh (c). However, since $\kappa_\mathrm{b} \gg \kappa_\mathrm{i}$, the solution is expected to be approximately isothermal inside the bare part Ω_b with most of the temperature difference across the insulation layer Ω_i. For this reason, it is desirable to keep the number of mesh elements inside Ω_b low in order to reduce the computational effort with negligible effect on the accuracy of the solution in Ω_b.

The computed temperature map for the five meshes are shown in figure 6 while maximum temperature, number of DoF and relative error for maximum model temperature are reported in table 3. Good agreement between the reference solution (a) and the TSA (e) can be observed. The unstructured coarse mesh (d) yields solutions with poor accuracy due to the bad conditioning of the mesh elements. The solution could be improved by (i) refining the mesh as in case (c) or (ii) using a structured mesh as in case (b), both resulting in higher quality mesh elements. However, (i) results in an increased number of DoF and (ii) requires additional geometry-dependent user-defined mesh constraints. This manual effort for the latter, to ensure a good mesh quality, is high for complex geometries. The TSA alleviates the problem of finding a suitable mesh representation of the thin volumetric layer and

Table 1. An overview of all model problems discussed in this paper or shared in [18].

Model name	A1	A2	A3	A4	B	C
Conductor arrangement	Two, simply touching				Four, in brick wall	One, HTS pancake coil
Visualization	Figure 1	[18]	[18]	Figure 1	Figure 4	Figure 7
Purpose	Derivation & implementation examples				Avoiding poor mesh quality using TSA	Solution time decrease using TSA
Results discussed here	No				Yes	Yes
Code available at [18]	Yes				No	No
Non-linear materials	No	No	No	Yes	No	Yes
Time-dependency	Yes				No	Yes
Quench heater	No	No	Yes	No	No	No
TSA with heat flux BC	No				Yes	No
TSA with temperature BC	No	Yes	Yes	No	No	No

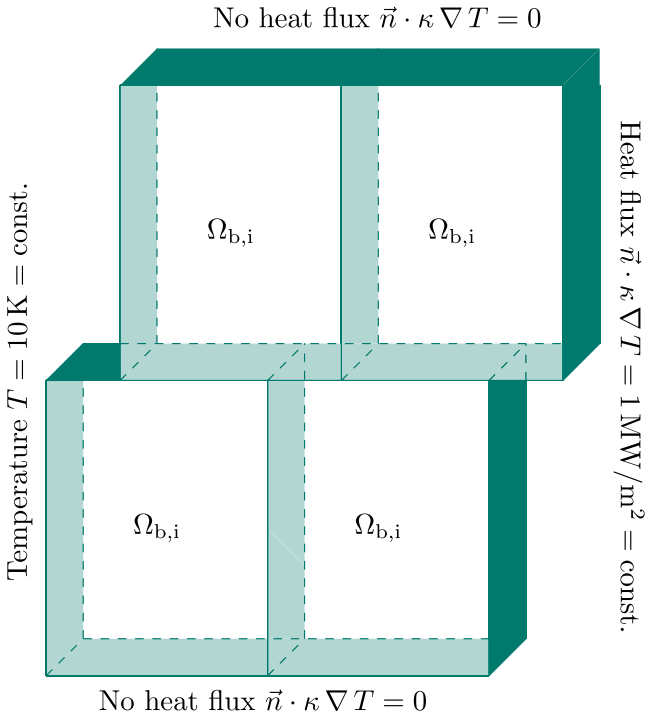

Figure 4. Model B; non-homogeneous BC are applied on the left and right bounding surfaces while homogeneous Neumann conditions impose zero heat flux on all other bounding surfaces. The volumetric insulation is depicted as a green surface, i.e. the TSA case.

Table 2. Model B; thermal conductivities in W m^{-1} K^{-1} for the brick wall example.

κ_{b}	κ_{i}
300	0.5

hence (i) significantly reduces the effort for meshing as well as (ii) potentially allows to use fewer DoF while retaining sufficient accuracy. The latter is demonstrated in the next subsection on an insulated HTS pancake coil geometry and mesh.

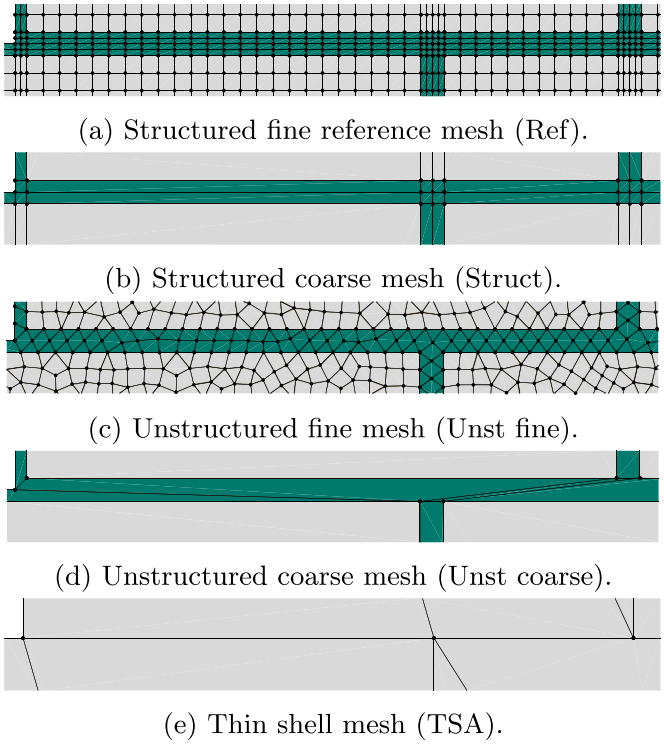

Figure 5. Parts of model B; the five different meshes investigated. For the sake of compactness and clear visualization, only the left part of the middle insulation layer is shown. Some edges of the hexahedra are non-orthogonal to the insulation edges due to an unstructured mesh (e).

4.3. Insulated HTS pancake coil

An insulated turns 3D HTS pancake coil is considered in this section and illustrated in figure 7. The HTS CC is modeled as a homogenized volume as detailed in B.1 with geometrical and material properties listed in table 4. The insulation layer is once volumetrically meshed as a reference as well as collapsed to a surface using the proposed TSA. Homogeneous Neumann conditions have been assumed everywhere on $\partial\Omega$ since the pancake is modeled as adiabatic.

A transient thermal simulation is considered and the pancake coil is heated in a defect region $\Omega_{\mathrm{defect}} \subset \Omega_{\mathrm{b}}$ (or $\Omega_{\mathrm{defect}} \subset \Omega_{\mathrm{b,i}}$) by a constant power density due to a local

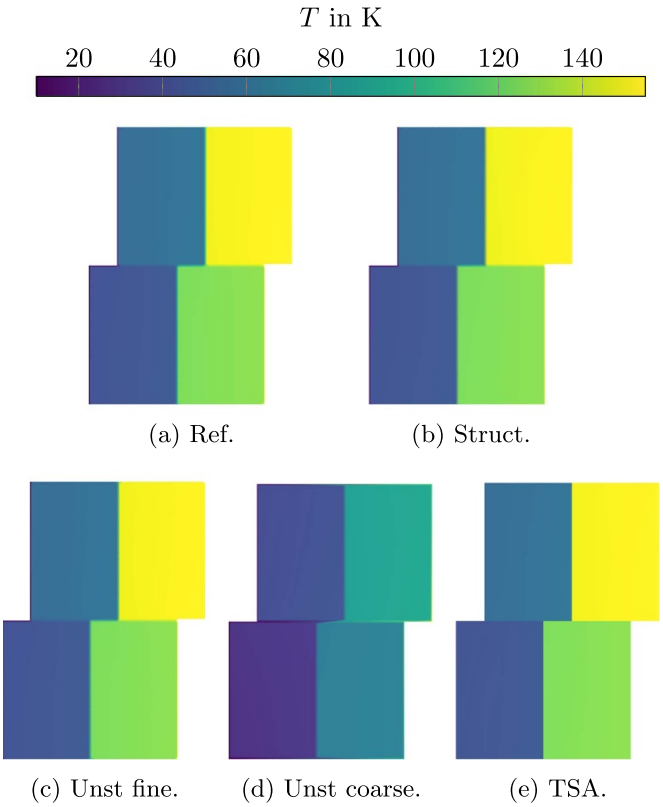

Figure 6. Model B; the computed 2D slice of temperatures for the brick wall geometry for the five meshes considered. The same scale range is used for all maps.

Table 3. Model B; computed maximum temperature, relative error of the maximum temperature with respect to the solution for the reference mesh and number of DoF for the five meshes.

Mesh (Figure 5)	max(T) in K	Rel. error max(T) in %	# DoF per extrusion layer
(a) Ref	154.75	Reference solution	9301
(b) Struct	153.27	0.96	63
(c) Unst fine	154.44	0.2	9374
(d) Unst coarse	92.08	41	31
(d) TSA	154.14	0.39	31

J_c degradation with $J_{c,\,\mathrm{defect}} = 0\,\mathrm{A\,mm^{-2}}$ (figure 8). Above the current sharing temperature T_{cs}, power starts to be dissipated and increase linearly up to the critical temperature T_c, i.e.

$$Q(\vec{x},T) = \begin{cases} \frac{1}{\sigma_b(T)} J_b^2, & \text{if } \vec{x} \in \Omega_{\mathrm{defect}}, \\ f_q(T)\frac{1}{\sigma_b(T)} J_b^2, & \text{if } \vec{x} \in \Omega_{b(,i)} \setminus \Omega_{\mathrm{defect}}, \\ 0, & \text{otherwise}, \end{cases} \tag{11}$$

with the position in space $\vec{x}$ and the transport current density J_b. Furthermore, the fraction of J_b flowing in a resistive way reads,

$$f_q(T) = \begin{cases} 0, & \text{if } T < T_{cs}, \\ \frac{T-T_{cs}}{T_c-T_{cs}}, & \text{if } T_{cs} \leqslant T \leqslant T_c, \\ 1, & \text{otherwise}, \end{cases} \tag{12}$$

and the effective electrical conductivity σ_b of the CC is defined in B.1. Model parameters regarding excitation, background field and the pancake coil design are given in table 5. The simulation is stopped once the temperature $T_{stop} = 250\,\mathrm{K}$ is reached.

First, the influence of the insulation thickness between the turns $\mathrm{th_i}$ will be studied for three values $\mathrm{th_i} \in \{40, 80, 120\}\ \mu\mathrm{m} \approx \{\frac{1}{3}, \frac{2}{3}, 1\}\ \mathrm{th_b}$ at the bare CC thickness $\mathrm{th_b}$. In order to account for the increased size of $\Omega_{b,i}$ compared to Ω_b, the material parameters of the insulation layer are modified as explained in B.2.

Figure 9 shows the temperature map computed for $\mathrm{th_i} = 40\,\mu\mathrm{m}$. Due to the low thermal conductivity of the insulation, only a small number of neighboring turns of the local defect also heat up significantly. Furthermore, good qualitative and quantitative agreement can be observed between the reference volumetric and TSA results with the relative error $\varepsilon_{\mathrm{rel}}$ between the reference and TSA model below 2 % in all coil regions for the final time step as seen in figure 9(b).

The evolution of the maximum temperature inside the coil is shown in figure 10(a), for the three investigated insulation layer thicknesses $\mathrm{th_i}$. The TSA and the reference solutions are

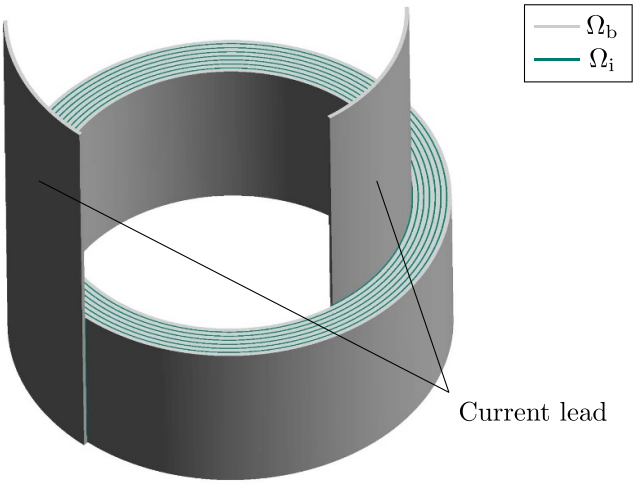

Figure 7. Model C; HTS pancake coil, the coated CC Ω_b is shown in grey whereas the insulation layer Ω_i is depicted as green. Only eight turns are shown for the sake of illustration and the current leads to the exterior boundary required for electromagnetic simulations are depicted as well, although not strictly needed for the thermal problem.

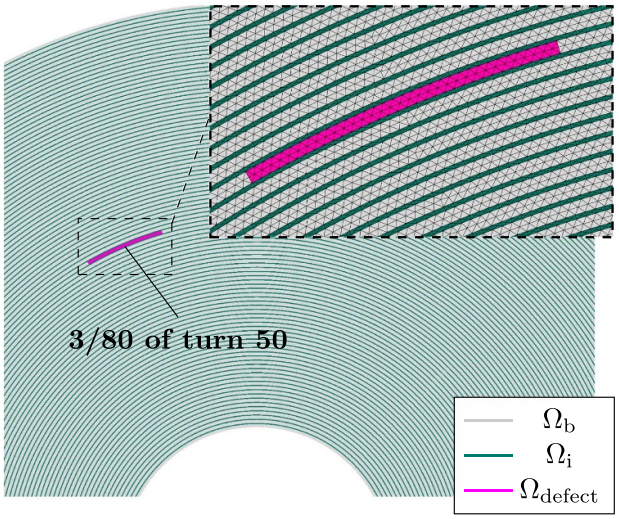

Figure 8. Model C; the local defect Ω_{defect} in turn 50 out of 100 turns is depicted in magenta and spans $3/80$ of the full turn. For the sake of a simple visualization, a top view is shown. Furthermore, a zoom in the fine volumetric insulation reference mesh used for $th_i = 40\,\mu$m is depicted.

Table 4. Model C; properties and parameters of the insulated CC.

Description	Value
Conductor manufacturer	Shanghai Creative Superconductor Technology
Conductor type	2G HTS rare-earth barium copper oxide (ReBCO) CC [26]
Bare conductor height	5 mm
ReBCO thickness	1 μm
Copper thickness	40 μm [27]
Hastelloy®-C276™ thickness	80 μm [28]
Silver thickness	1 μm [29, 30]
Kapton insulation thickness between turns th_i	40 μm or 80 μm or 120 μm [27]
Current sharing temperature at $B_{ext} = 5$ T	25 K [31]
Critical temperature at $B_{ext} = 5$ T	80 K [31]
Critical current at $B_{ext} = 5$ T and $T_{init} = 15$ K	368 A [31]

Table 5. Model C; model parameters used for the simulation of the insulated HTS pancake coil.

Description	Value
Transport current, I_b	210 A
External field, B_{ext}	5 T parallel to coil axis
Initial temperature, T_{init}	15 K
Cooling condition	Adiabatic
Number of turns	101
Inner radius	5 mm

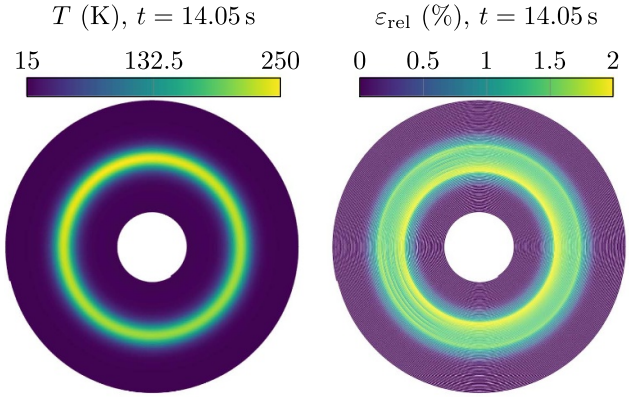

(a) Final temperature distribution (TSA).

(b) Rel. error ε_{rel} between TSA and reference.

Figure 9. Model C; (a) final temperature distribution caused by thermal runaway of a local defect for the insulated HTS coil with $th_i = 40\,\mu$m, (b) relative temperature error between volumetric insulation reference and TSA.

in good agreement for all th_i and show the typical temperature evolution of a local hot spot of a HTS coil; a slow temperature increase followed by fast thermal runaway [32]. Furthermore, it can be observed that the thermal runaway occurs earlier if th_i is larger. For thicker insulation, less heat is conducted in the radial direction across the insulation and thus, the local hot spot temperature increases more quickly. Figure 10(b) shows the relative difference between both models. Again, excellent agreement is observed for all investigated insulation thicknesses with relative errors below 2% for all time steps.

With the last numerical experiments, we have verified the TSA model against volumetric meshed FE simulations. As a last experiment, the reduction in computational time and number of DoF required for the same solution accuracy will be highlighted. To this end, let us investigate the influence of the ratio of insulation thickness to the thickness of the bare CC, i.e.

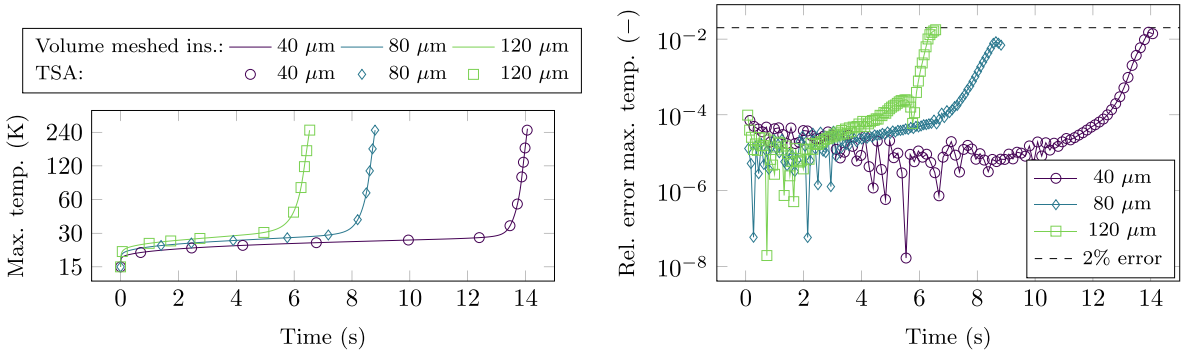

(a) Time evolution of the maximum temperature.

(b) Relative difference between TSA and vol. meshed ins.

Figure 10. Model C; (a) time evolution of the maximum temperature and (b) relative maximum temperature difference, both for TSA and volumetrically meshed reference for the insulated HTS pancake coil for different insulation thicknesses $\mathrm{th_i}$.

$$r_{\mathrm{th}} = \frac{\mathrm{th_i}}{\mathrm{th_b}}, \tag{13}$$

with $\mathrm{th_b}$ fixed to $\mathrm{th_b} = 121\,\mu$m. We then determine the number of DoF $n_{\mathrm{DoF,\,5\%,\,ref}}$ ($n_{\mathrm{DoF,\,5\%,\,TSA}}$) and solution time $\mathrm{st}_{5\%,\,\mathrm{ref}}$ ($\mathrm{st}_{5\%,\,\mathrm{TSA}}$) for the reference (TSA) model required to reach a relative error of under 5% with respect to a fine reference solution with volumetric insulation at $T_{\mathrm{eval}} = 100$ K.

In figure 11, the ratios between the latter:

$$r_{\mathrm{DoF,\,5\%}} = \frac{n_{\mathrm{DoF,\,5\%,\,TSA}}}{n_{\mathrm{DoF,\,5\%,\,ref}}} \tag{14}$$

and

$$r_{\mathrm{st,\,5\%}} = \frac{\mathrm{st}_{5\%,\,\mathrm{TSA}}}{\mathrm{st}_{5\%,\,\mathrm{ref}}} \tag{15}$$

are depicted as a function of r_{th}. The benefit in terms of reduction of simulation time when using the TSA model increases as r_{th} decreases. No significant benefit is recorded for values of r_{th} close to one while for the lowest value of r_{th} investigated, the TSA reduces the required solution time and number of DoF by about three times. This is caused by (i) the influence of mesh elements of poor quality inside the volumetric insulation layer on the numerical solution, as highlighted in section 4.2, requiring a finer mesh to improve its quality and (ii) problems in the automatic creation of suitable meshes which partially prevent the creation of coarser meshes in the volumetric insulation layer. Let us note that these problems, in particular the latter, can be mitigated or even be avoided if appropriate user-defined mesh constraints are imposed. As mentioned before, however, this does not provide a general approach in particular requiring significant manual effort for each change of the coil geometry.

The magnetic field also needs to be computed for a comprehensive quench simulation. If there are no eddy currents and the model magnetic field depends linearly on the coil current, a single magnetostatic solution could be used proportionally with the current. However, for general non-linear magnetic field dependence on the current (e.g. for NI coils or non-linear B-H), the magnetoquasistatic subset of Maxwell's equations needs to be solved. If the latter equations are to be solved using

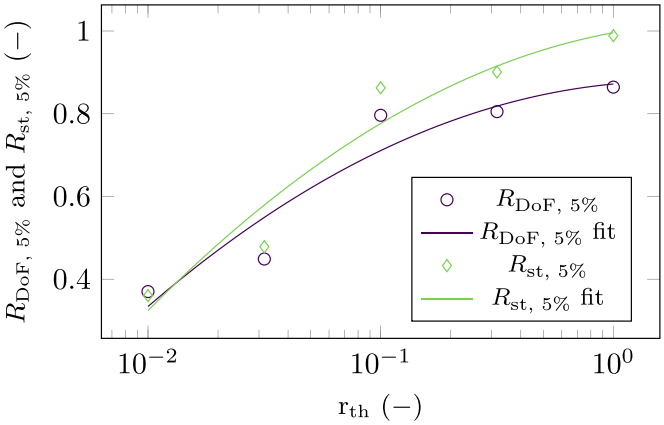

Figure 11. Model C; the computational benefit in terms of decreased solution time and number of DoF when using the TSA as a function of the ratio of the insulation to the conductor thickness. The data points depict the number of DoF and solution time required to reach a relative temperature error below 5% at $T_{\mathrm{eval}} = 100$ K with respect to a fine reference solution with volumetric mesh of the insulation layer. A quadratic least-squares fit of the data points is shown as well.

FE, the air region surrounding the coil needs to be meshed as well and fine mesh sizes of the thin volume insulation layers will propagate to the latter region, increasing further the observed mesh quality issues.

Furthermore, for NI HTS pancake coils, $r_{\mathrm{th}} \to 0$, making meshed insulation a non-practical alternative. This is highlighted in figure 12 which shows the absolute number of DoF corresponding to the data points of figure 11, i.e. the number of DoF required to reach a relative temperature error below 5%. While it only slightly increases for the TSA as rth is decreasing, the reference volumetric mesh model shows a strong dependence on the latter. An additional data point has been added for the TSA, this time using a fine TSA model as the reference as a volumetric insulation reference is not available due to the low rth. This is one of the the main benefits of the proposed TSA which allows the FE solution of problems with vanishing turn-to-turn distance such as NI coils, where a classical FE approach requires a non-practical mesh for the

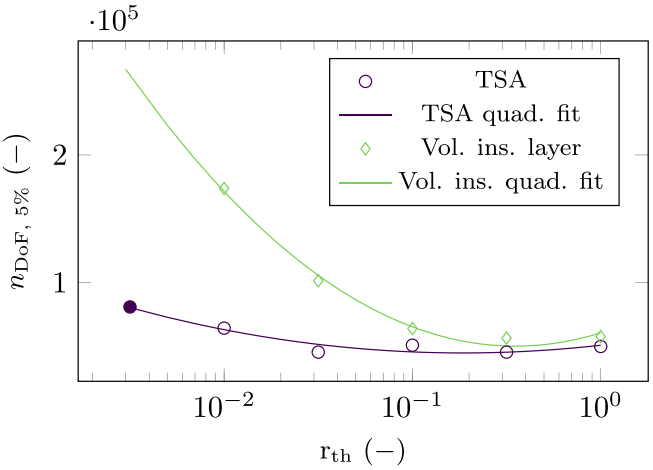

Figure 12. Model C; the number of DoF required to reach an error below 5% at $T_{\mathrm{eval}} = 100\,\mathrm{K}$ with respect to a fine reference solution with volumetric insulation mesh. A quadratic least-squares fit of the data points is shown. For the lowest value of r_{th} depicted, no reference solution is available and the corresponding data point for the TSA marked in solid black has been computed with respect to a TSA model with fine mesh.

distance between turns tending towards zero. For NI coils, the thermal turn-to-turn contact resistance could be modeled using the thermal TSA as proposed in this work while the electric contact resistance could be modeled using the magnetic TSA as proposed in [11].

5. Conclusion

In this paper, a thermal TSA for 3D FE simulations has been presented which uses a 1D FE discretization across the thickness of the thin shell. The approximation avoids the need for meshing thin volumetric layers by collapsing them into surfaces thus significantly reducing the required effort for geometry creation and meshing. Due to the use of a 3D tensor-product FE discretization of the thin layer, the proposed formulation is of general nature and not restricted to superconducting electromagnets.

The derived formulation has been implemented in an open-source FE framework with Gmsh and GetDP. A reference implementation of a simple example problem is distributed alongside this paper showing all details of the implementation of the formulation.

The influence of the mesh quality on the numerical accuracy of the computed solution has been highlighted for the brick wall example. It is shown that effort needs to be put into the creation of a high-quality mesh representation of the thin layer in order to retain accurate results. The proposed TSA alleviates this need and yields accurate results with reduced effort for mesh creation.

The formulation has been verified against a reference solution with meshed insulation for an insulated HTS pancake coil for different insulation thicknesses. The typical rapid thermal runaway after slow temperature increase has been captured accurately with the proposed TSA formulation. The influence of the insulation thickness on the evolution of the thermal hot spot temperature over time has been studied and is in agreement with meshed insulation reference solutions.

Last, the required number of DoF and solution time has been shown as a function of the ratio of insulation thickness to conductor thickness. If the latter is small, the thin shell approximation yields accurate results with significantly lower computational effort. This makes the TSA especially interesting for the simulation of NI HTS pancake coils for which the distance between the turns tends to zero.

Data availability statement

The data cannot be made publicly available upon publication because they are not available in a format that is sufficiently accessible or reusable by other researchers. The data that support the findings of this study are available upon reasonable request from the authors.

Acknowledgment

The authors would like to thank Bruno de Sousa Alves (formerly École Polytechnique de Montréal), Christophe Geuzaine, Julien Dular, Benoît Vanderheyden (all Université de Liège) and Nicolas Marsic (formerly Technical University of Darmstadt) for the fruitful discussions on simulation of superconductors.

The work of Erik Schnaubelt has been sponsored by the Wolfgang Gentner Programme of the German Federal Ministry of Education and Research (grant no. 13E18CHA) and by the Graduate School CE within the Centre for Computational Engineering at the Technical University of Darmstadt.

Appendix A. Derivation of decomposition of internal problem

In this section, all terms of the internal FE discretization are derived in detail. Using $\nabla(T_j N_j) = T_j \nabla N_j + N_j \nabla T_j$, $\nabla T_j \cdot \nabla N_l = 0$ and setting $l = k-1, k$, we find that:

$$
\begin{aligned}
(\kappa \nabla T, \nabla T')_{\hat{\Omega}_{\mathrm{i}}^{(k)}} &= \sum_{j=k-1}^{k} \left(\kappa \nabla (T_j N_j), \nabla (T_l' N_l)\right)_{\hat{\Omega}_{\mathrm{i}}^{(k)}} \\
&= \sum_{j=k-1}^{k} (\kappa T_j \nabla N_j, T_l' \nabla N_l)_{\hat{\Omega}_{\mathrm{i}}^{(k)}} \\
&\quad + \sum_{j=k-1}^{k} (\kappa N_j \nabla T_j, N_l \nabla T_l')_{\hat{\Omega}_{\mathrm{i}}^{(k)}} \\
&= \sum_{j=k-1}^{k} \langle S_{lj,\kappa}^{(k)} T_j, T_l' \rangle_{\Gamma_{\mathrm{i}}^{(k)}} \\
&\quad + \sum_{j=k-1}^{k} \langle M_{lj,\kappa}^{(k)} \nabla T_j, \nabla T_l' \rangle_{\Gamma_{\mathrm{i}}^{(k)}}.
\end{aligned}
$$

In the last step, the 1D FE stiffness and mass matrices:

$$S^{(k)}_{lj,\kappa} := \int_{w_{k-1}}^{w_k} \kappa\, \partial_w N_l\, \partial_w N_j \,\mathrm{d}w, \tag{A.1}$$

$$M^{(k)}_{lj,\kappa} := \int_{w_{k-1}}^{w_k} \kappa N_l N_j \,\mathrm{d}w, \tag{A.2}$$

are introduced. Likewise, we find:

$$\begin{aligned}(C_\mathrm{V}\,\partial_t T, T')_{\hat{\Omega}_\mathrm{i}^{(k)}} &= \sum_{j=k-1}^{k} \left(C_\mathrm{V}\,\partial_t\left(T_j N_j\right), T_l' N_l\right)_{\hat{\Omega}_\mathrm{i}^{(k)}} \\ &= \sum_{j=k-1}^{k} \langle M^{(k)}_{lj,C_\mathrm{V}}\,\partial_t T_j, T_l'\rangle_{\Gamma_\mathrm{i}^{(k)}},\end{aligned}$$

with the 1D matrix:

$$M^{(k)}_{lj,C_\mathrm{V}} := \int_{w_{k-1}}^{w_k} C_\mathrm{V} N_l N_j \,\mathrm{d}w. \tag{A.3}$$

Last, we have:

$$(Q, T')_{\hat{\Omega}_\mathrm{i}^{(k)}} = (Q, T_l' N_l)_{\hat{\Omega}_\mathrm{i}^{(k)}} = \langle f^{(k)}_{l,Q}, T_l'\rangle_{\Gamma_\mathrm{i}^{(k)}},$$

with the 1D matrix:

$$f^{(k)}_{l,Q} := \int_{w_{k-1}}^{w_k} Q N_l \,\mathrm{d}w. \tag{A.4}$$

Appendix B. Insulated HTS pancake coil: effective material properties and scaling

In this section, the effective material properties as well as scaling used for the TSA are introduced for model C, the insulated HTS pancake coil.

B.1. Effective material properties

For the homogenization of the CC Ω_b and $\Omega_{\mathrm{b,i}}$, the effective material parameters are computed as [33]:

$$C_\mathrm{V}|_{\Omega_\mathrm{b}} = C_\mathrm{V}|_{\Omega_{\mathrm{b,i}}} = \sum_j f_j C_{\mathrm{V},j}, \tag{B.1}$$

$$\kappa|_{\Omega_\mathrm{b}} = \kappa|_{\Omega_{\mathrm{b,i}}} = \sum_j f_j \kappa_j, \tag{B.2}$$

$$\sigma_{\mathrm{b,i}} = \sigma_\mathrm{b} = \sum_j f_j \sigma_j, \tag{B.3}$$

with the volumetric fraction f_j of layer j of the multi-layered CC. Let us note that equation (B.2) computes the parallel thermal conductivity in analogy with an electrical circuit. This choice has been made since (i) the length of the CC is considerably larger than its thickness and thus, the temperature gradient in thickness direction inside Ω_b and $\Omega_{\mathrm{b,i}}$ can be assumed to be negligible (as opposed to the non-zero temperature difference across the insulation Ω_i, i.e. between two turns) and (ii) in order to keep an isotropic material property. However, the TSA formulation and implementation could handle anisotropic materials inside $\Omega_{\mathrm{b,i}}$ as well.

B.2. Problem-dependent scaling of material parameters

In this section, the scaling of the material parameters of the insulation layer of the HTS pancake coil is described. Using the scaling factor:

$$p = \frac{|\Omega_\mathrm{b}| + |\Omega_\mathrm{i}|}{|\Omega_\mathrm{b}|} = 1 + \frac{|\Omega_\mathrm{i}|}{|\Omega_\mathrm{b}|}, \tag{B.4}$$

which represents the relative volume ratio of the conductor including insulation compared to the bare conductor, the material parameters of the insulation are scaled by:

$$\kappa_{\mathrm{i,\,scaled}} = p\,\kappa_\mathrm{i} \quad \text{and} \quad C_{\mathrm{V,\,i,\,scaled}} = p\,C_{\mathrm{V},i}.$$

Obviously, if $\dfrac{|\Omega_\mathrm{i}|}{|\Omega_\mathrm{b}|} \to 0$ then $p \to 1$ which ensures the consistency of the scaling.

ORCID iDs

Erik Schnaubelt https://orcid.org/0000-0003-3224-6729
Mariusz Wozniak https://orcid.org/0000-0002-3588-426X
Sebastian Schöps https://orcid.org/0000-0001-9150-0219

References

[1] Bortot L, Auchmann B, Cortes Garcia I, Fernando Navarro A M, Maciejewski M, Mentink M, Prioli M, Ravaioli E, Schöps S and Verweij A 2018 STEAM: a hierarchical co-simulation framework for superconducting accelerator magnet circuits *IEEE Trans. Appl. Supercond.* **28** 3

[2] Cortes Garcia I, Schöps S, Bortot L, Maciejewski M, Prioli M, Fernandez Navarro A M, Auchmann B and Verweij A 2017 Optimized field/circuit coupling for the simulation of quenches in superconducting magnets *IEEE J. Multiscale Multiphys. Comput. Tech.* **2** 97–104

[3] D'Angelo L A M, Späck-Leigsnering Y and De Gersem H 2022 Quasi-3D magneto-thermal quench simulation scheme for superconducting accelerator magnets *IEEE Trans. Appl. Supercond.* **32** 1–5

[4] Driesen J, Belmans R and Hameyer K 2001 Finite-element modeling of thermal contact resistances and insulation layers in electrical machines *IEEE Trans. Ind. Appl.* **37** 15–20

[5] Monk P 2003 *Finite Element Methods for Maxwell's Equations* (Oxford: Oxford University Press)

[6] Ortwein R, Blocki J, Wachal P, Kirby G and van Nugteren J 2020 FEM modeling of multilayer Canted Cosine Theta (CCT) magnets with orthotropic material properties *Cryogenics* **107** 103041

[7] Boggs P T, Althsuler A, Larzelere A R, Walsh E J, Clay R L and Hardwick M F 2005 DART system analysis *Technical Report* (Sandia National Laboratories)

[8] Mayergoyz I and Bedrosian G 1995 On calculation of 3-D eddy currents in conducting and magnetic shells *IEEE Trans. Magn.* **31** 1319–24

[9] Krähenbühl L and Muller D 1993 Thin layers in electrical engineering. Example of shell models in analysing eddy-currents by boundary and finite element methods *IEEE Trans. Magn.* **29** 1450–5

[10] Guerin C, Tanneau G, Meunier G, Brunotte X and Albertini J-B 1994 Three dimensional magnetostatic finite

elements for gaps and iron shells using magnetic scalar potentials *IEEE Trans. Magn.* **30** 2885–8
[11] de Sousa Alves B, Lahtinen V, Laforest M and Sirois F 2021 Thin-shell approach for modeling superconducting tapes in the h-ϕ finite-element formulation *Supercond. Sci. Technol.* **35** 024001
[12] Bortot L, Auchmann B, Cortes Garcia I, De Gersem H, Maciejewski M, Mentink M, Schöps S, van Nugteren J and Verweij A 2020 A coupled A-H formulation for magneto–thermal transients in high-temperature superconducting magnets *IEEE Trans. Appl. Supercond.* **30** 5
[13] Chan W K, Masson P J, Luongo C and Schwartz J 2010 Three–dimensional micrometer–scale modeling of quenching in high–aspect–ratio $YBa_2Cu_3O_{7-\delta}$ coated conductor tapes–part I: model development and validation *IEEE Trans. Appl. Supercond.* **20** 2370–80
[14] Ern A and Guermond J-L 2004 *Theory and Practice of Finite Elements* (New York: Springer)
[15] Brenner S and Scott L 2002 *The Mathematical Theory of Finite Element Methods* (*Texts in Applied Mathematics*) (New York: Springer)
[16] Trevino C, Becerra G and Méndez F 1997 The classical problem of convective heat transfer in laminar flow over a thin finite thickness plate with uniform temperature at the lower surface *Int. J. Heat Mass Transfer* **40** 3577–80
[17] COMSOL Multiphysics® Version 5.5 Documentation 2022 Theoretical background of the different formulations (available at: https://doc.comsol.com/5.5/doc/com.comsol.help.heat/heat_ug_theory.07.23.html#695850) (Accessed 17 September 2022)
[18] Schnaubelt E Thermal thin shell approximation for finite element quench simulation 2022 (available at: https://zenodo.org/record/7129194)
[19] Geuzaine C, Dular P and Legros W 2000 Dual formulations for the modeling of thin electromagnetic shells using edge elements *IEEE Trans. Magn.* **36** 799–803
[20] Whiteley J (ed) 2017 *Finite Element Methods* (*Mathematical Engineering*) 1st edn (Basel: Springer)
[21] Ascher U M and Petzold L R 1998 *Computer Methods for Ordinary Differential Equations and Differential-Algebraic Equations* (Philadelphia, PA: SIAM)
[22] Dular P, Geuzaine C, Henrotte F and Legros W 1998 A general environment for the treatment of discrete problems and its application to the finite element method *IEEE Trans. Magn.* **34** 3395–8
[23] Geuzaine C and Remacle J-F 2009 Gmsh: A 3-D finite element mesh generator with built-in pre- and post-processing facilities *Int. J. Numer. Methods Eng.* **79** 1309–31
[24] Geuzaine C and Remacle J-F 2022 Documentation of the Gmsh python API (available at: https://gmsh.info/doc/texinfo/gmsh.html#Gmsh-API) (Accessed 15 July 2022)
[25] Geuzaine C and Remacle J-Fçois 2022 Documentation of the Gmsh crack plugin (available at: https://gmsh.info/doc/texinfo/gmsh.html#index-Plugin_0028Crack_0029) (Accessed 15 July 2022)
[26] Shanghai Superconductor 2022 Second generation high temperature superconducting tape (available at: http://www.shsctec.com/index.php?m=list&a=index&classid=62)
[27] Manfreda G 2011 *Review of ROXIE's material properties database for quench simulation* 1178007 CERN
[28] Lu J, Choi E S and Zhou H D 2008 Physical properties of Hastelloy®C-276™ at cryogenic temperatures *J. Appl. Phys.* **103** 064908
[29] Smith D and Fickett F 1995 Low-temperature properties of silver *J. Res. Natl Inst. Stand. Technol.* **100** 119–71
[30] Iwasa Y, McNiff E, Bellis R and Sato K 1993 Magnetoresistivity of silver over temperature range 4.2 – 159 K *Cryogenics* **33** 836–7
[31] Wimbush S and Strickland N 2017 Critical current characterisation of shanghai creative superconductor technologies 2G HTS superconducting wire (available at: https://figshare.com/articles/dataset/Critical_current_characterisation_of_Shanghai_Creative_Superconductor_Technologies_2G_HTS_superconducting_wire/5309947/1)
[32] Marchevsky M 2021 Quench detection and protection for high-temperature superconductor accelerator magnets *Instruments* **5** 3
[33] Xu Y, Tang Y, Ren L, Dai Q, Xu C, Wang Z, Shi J, Li J, Liang S and Yan S 2016 Numerical simulation and experimental validation of a cooling process in a 150-kJ SMES magnet *IEEE Trans. Appl. Supercond.* **26** 1–7